Ultrawide-range refractive-index sensor based on asymmetric integrated Y-junction optical waveguide

[1]Phongwisit P., [1,2]Kamoldilok S., [1]Limsuwan P. and [1,2*]Srinuanjan K.

[1] Department of Physics, School of Science, King Mongkut's Institute of Technology Ladkrabang, Bangkok 10520, Thailand, keerayoot.sr@kmitl.ac.th
[2] Devices and Systems for Energy and Environment Research Unit, School of Science, King Mongkut's Institute of Technology Ladkrabang, Bangkok 10520, Thailand

Received: 31.03.2023

Abstract. We present a novel ultrawide-range refractive index (RI) sensor based on an asymmetric Y-junction optical splitter. A cylindrically shaped rod with a diameter of 350 nm and a height of 1000 nm with a different RI is inserted into a junction of the asymmetric Y-junction waveguide. This rod serves as a sensing area. Our sensor is simulated using a finite-difference time-domain technique. The splitting ratio is studied for the cases of two operating wavelengths, 1480 and 1550 nm. The results show that the splitting ratio can be described as a parabolic function of the RI of the sensing area at both operating wavelengths. An approximately linear relationship between the splitting ratio and the RI occurs in a narrower RI region of 1.00–1.50, thus enabling to design an ultrawide-range RI sensor. The sensor sensitivities at the wavelengths 1480 and 1550 nm are equal respectively to 0.2653 and –0.4908 RIU^{-1}, with the corresponding R^2 parameters amounting to 0.9889 and 0.9777. Our device can serve as an ultrawide-range optical RI sensor for identification of micro-scale biochemical or chemical specimens.

Keywords: refractive-index sensors, intensity-shift sensors, Y-junction waveguides, integrated photonics

UDC: 681.586.5

1. Introduction

Traditional optical methods for analyzing biochemical or chemical specimens are based on their unique infrared-absorption fingerprints obtained with absorption spectrometry [1–5]. The alternative approaches used for identification is to measure the refractive index (RI) of a specimen with an RI sensor. While the absorption spectrometry uses a specific absorption value of a specimen predicted by the Beer–Lambert law as a function of light wavelength and its comparison with a standard database, the more recent concept of RI sensors is based on a change observed in the RI of a specimen, which changes the conditions of light propagation. Shifts in the optical spectra play an important role in the mechanism of some RI sensors. This type of the sensors, which are called spectral-shift RI sensors, rests upon the shifts observed in the optical transmission spectra which result from resonance or interference effects. A number of specific designs of those sensors have been offered, which are based on a Michelson interferometer [6], a Mach–Zehnder interferometer [7], photonic crystals [8, 9], a so-called PANDA ring resonator [10], resonant-based micro-cavities [11, 12], and a surface plasmon resonance effect [13–15].

The spectral-shift RI sensors are interesting because of their compact size, high selectivity and suitability for real-time detection, whereas the absorption spectrometry is excellent in its high sensitivity, reliability and selectivity. The sensors mentioned above require either a broadband

*Corresponding author

light source or an optical spectrum analyzer – or both of them [16, 17]. Note that these facilities are costly and require meticulous modes of their operation.

Another type of the RI sensors called as intensity-shift sensors has been introduced recently. These sensors require a few pieces of equipment [18–24]. In particular, they require only a narrow-bandwidth light source (e.g., a laser diode) and a photodetector. The RI of a given specimen can be measured by analyzing the output intensity of light, which corresponds to the changing RI of the specimen located in a sensing area. A lot of such RI sensors have been designed in the last decade. They are based on different configurations of optical-fibre structures, e.g. long-period fibre gratings [18], plastic optical fibres [19], and so-called SNHNS [20] or TMDM [21] waveguide structures. Besides of the structures associated with optical fibres, the intensity-shift RI sensors based on specific photonic waveguide structures have also been reported, such as nanowire waveguides [22], cavity-coupled metallic nanoparticles [23] or two-dimensional materials [24]. The idea of intensity shift gives a chance to create compact-size RI sensors for many applications in the medical and industrial fields. Unfortunately, most of them can be operated only in a narrow range of RI values.

The principles of Y-junction (or Y-branch) waveguides are now widely used by researchers, although mostly for optical communications [25–28]. In the present study, we consider an asymmetric Y-junction waveguide as an RI sensor. As a result, an ultrawide-range intensity-shift RI sensor with a novel design can be introduced. This sensor is based on an asymmetric Y-junction optical splitter with a rod-like sensing area where a specimen is located. The appropriate sensing mechanism is a change in the splitting ratio at a given operating light wavelength, which corresponds to the RI changes occurring in the rod-like sensing area. A theoretical model of the sensor is simulated using a known finite-difference time-domain (FDTD) approach. Our simulation results have revealed a general parabolic relationship between the RI of the sensing area and the splitting ratio. In particular, an almost perfect linear relationship has been obtained for our intensity-shift RI sensor in the narrower region 1.00–1.50 of RI values. In this way we confirm that our device can serve as an ultrawide-range intensity-shift RI sensor for investigating various biochemical or chemical specimens. Moreover, the structure of our sensor is simple and does not require a broadband light source or an optical spectrum analyzer. Only a rod-like sensing area integrated into the asymmetric Y-junction waveguide, a laser diode and a photodetector are needed.

2. Methods used for analyzing an ultrawide-range optical RI sensor

In this Section we describe the methods used for our analysis. An optical waveguide has been designed and simulated with commercial software, OptiFDTD. This program simulates the optical propagation based on the FDTD method [29]. After finishing the simulation process, we have analyzed the results obtained for the optical transmission at each output port and the splitting ratio of the waveguide. The relationship between the splitting ratio and the RI changes in the sensing area can be represented mathematically in either parabolic or, under some conditions, linear form.

2.1. Principles of optical splitters

Optical power splitters and directional couplers can be analyzed with a method of scattering matrix (S-matrix) for a two-port network (see Ref. [30] and a diagram in Fig. 1). Then the electromagnetic field at the output port can be given by the following equation:

$$\begin{vmatrix} E_{out1} \\ E_{out2} \end{vmatrix} = \begin{vmatrix} S_{11} & S_{12} \\ S_{21} & S_{22} \end{vmatrix} \begin{vmatrix} E_{in1} \\ E_{in2} \end{vmatrix}, \tag{1}$$

where E_{in1} and E_{in2} are the electromagnetic fields respectively at the input ports 1 and 2, and

E_{out1} and E_{out2} denote the electromagnetic fields respectively at the output ports 1 and 2. Here S_{ij} implies the *S*-parameter of the electromagnetic field in the coupling region which is located in between the input port *j* and the output port *i*.

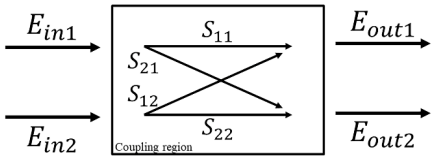

Fig. 1. A scheme of a two-port network.

The optical transmission at each port is related to the electromagnetic fields as follows:

$$T_1 = \left|E_{out1}\right|^2 = S_{11}^2 \left|E_{in1}\right|^2 + S_{12}^2 \left|E_{in2}\right|^2, \tag{2}$$

$$T_2 = \left|E_{out2}\right|^2 = S_{21}^2 \left|E_{in1}\right|^2 + S_{22}^2 \left|E_{in2}\right|^2, \tag{3}$$

where T_1 and T_2 are the intensities associated with the optical transmissions at the output ports 1 and 2, respectively. The splitting ratio of a splitter can be obtained as the ratio of the transmitted intensity at the output port 1 to the transmitted intensity at the output port 2:

$$Splitting\ ratio = \frac{T_1}{T_2}. \tag{4}$$

A concept of sensitivity can be used to analyze the performance of a sensor. The sensitivity is the ratio of the change found in the measured splitting ratio at the output (Δ_{output}) to the RI change at the input (Δ_{input}) [31]:

$$Sensitivity = \frac{\Delta_{output}}{\Delta_{input}} = \frac{Splitting\ ratio}{n}, \tag{5}$$

where n is the RI of a rod-like sensing area. The sensitivity is measured as the splitting ratio per the RI unit (RIU), or in RIU^{-1}.

2.2. Asymmetric Y-junction optical splitter

Using the S-matrix, one can rewrite the transmitted intensity for the asymmetric Y-junction optical splitter in terms of the parameters referred to a single input port and two output ports:

$$T_1 = \left|E_{out1}\right|^2 = S_{11}^2 \left|E_{in1}\right|^2, \tag{6}$$

$$T_2 = \left|E_{out2}\right|^2 = S_{21}^2 \left|E_{in1}\right|^2. \tag{7}$$

In this work, we define S_{11}^2 as $1-\kappa$. Then we obtain $S_{21}^2 = \kappa$ from the *S*-matrix, where κ is the coupling coefficient. It can be obtained from the simulation results for the transmitted intensity and the RI change in the coupling region. The optical transmission at each port is related to the electromagnetic field:

$$T_1 = \left|E_{out1}\right|^2 = (1-\kappa)\left|E_{in1}\right|^2, \tag{8}$$

$$T_2 = \left|E_{out2}\right|^2 = \kappa \left|E_{in1}\right|^2. \tag{9}$$

Then the splitting ratio for the asymmetric Y-junction optical splitter reads as follows:

$$Splitting\ ratio = \frac{T_1}{T_2} = \frac{1-\kappa}{\kappa}. \tag{10}$$

The splitting ratio and the coupling coefficient have been studied as functions of the operating wavelength and the RI of the coupling region. These parameters have been derived from the FDTD simulation results. Then the relations for the splitting ratio and the coupling coefficient have been examined.

As already mentioned above, we have designed our optical splitter on an asymmetric Y-junction waveguide structure [32]. Indium phosphide is used as a waveguide core. The RI of the core is equal to $n_{core} = 3.16$. The core is surrounded by air as a cladding and a substrate, with the RI being equal to $n_{clad} = n_{substrate} = 1.00$. The cross-section of the splitter is characterized by the width 1 μm and the height 1 μm. The distance between the input port and the output port 1 amounts to 13 μm and the distance between the junction and the output port 2 is 6 μm. The branching angle between each of output ports is 45° and the other features of the splitter structure are shown in Fig. 2.

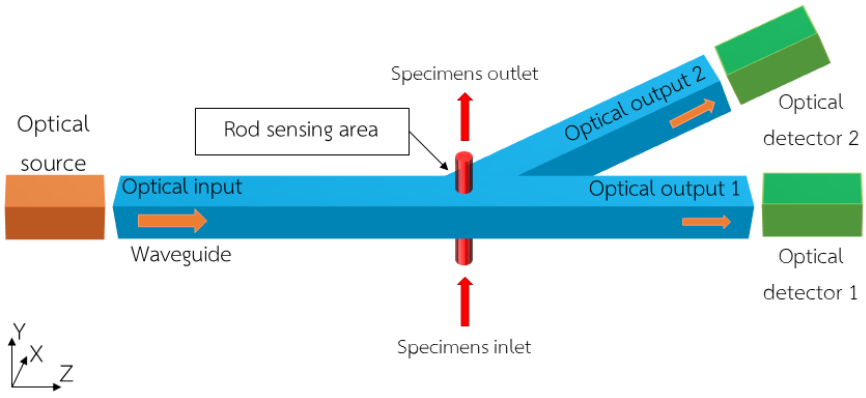

Fig. 2. Schematic design of our RI sensor based on the asymmetric Y-junction waveguide.

A cylindrically shaped rod-like sensing area has been put into the junction of the waveguide as a coupling region. The diameter and the height of the sensing area are equal to 350 nm and 1000 nm, respectively. Its RI of the sensing area has been varied in the overall range 1.00–2.50. A specimen can be injected into the sensing area with a nano-mixer or nano-injector, using nano- or micro-electromechanical technologies [33]. The effect of the RI change on the intensity shift has been studied for two different operating wavelengths, $\lambda_1 = 1480$ nm and $\lambda_2 = 1550$ nm, of the TE mode in the waveguide. The optical transmissions at both wavelengths are split according to the unit splitting ratio whenever the sensing area is filled with air (the RI $n = 1.00$). At any other RI value, the optical transmissions are split according to the other ratios, such that the dependence of this parameter on the RI is parabolic or, in a particular RI region, it acquires a simple linear form. The linear relationship would in fact imply an ultrawide-range RI sensor.

3. Results and discussion

In the present Section, we report the results for the splitting ratio, the sensitivity, the standard R^2 parameter and the coupling coefficient, which have been obtained from the simulation process.

3.1. Simulation results for the overall RI range

According to the simulations, we have obtained the splitting ratios as functions of the RI at both operating wavelengths (see Fig. 3). The two dependences can be fitted by a parabola with sufficiently high accuracies (the goodness-of-fit parameters R^2 being 0.9761 and 0.9884 respectively for the wavelengths 1480 and 1550 nm).

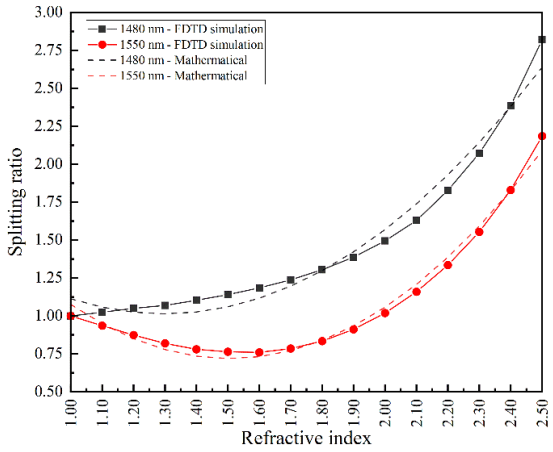

Fig. 3. Simulated splitting ratios as functions of RI changing in the range 1.00–2.50: black squares and red circles correspond respectively to the operating wavelengths 1480 and 1550 nm, and dash curves are the data calculated with Eq. (11).

The splitting ratio at the operating wavelength 1480 nm increases from 1.00 to 2.82 when the RI increases from 1.00 to 2.50. On the other hand, the splitting ratio at 1550 nm decreases with increasing RI in the region 1.00–1.60. After that we have an increasing behaviour in the RI region 1.60–2.50. The minimal splitting ratio, 0.76, is obtained at the RI equal to 1.60 and the maximal ratio of 2.18 takes place at the RI value 2.50.

The dependences of the splitting ratio on the RI at different operating wavelengths have been fitted by a quadratic function:

$$Splitting\ ratio(n,\lambda) = \alpha\lambda\left(n-\beta\lambda\right)^2 + \gamma\lambda, \tag{11}$$

where n is the RI of a rod-like sensing area, λ the operating wavelength, and the parameters $\alpha = 3.7900\times10^6 - 4.4861/\lambda_{1,2}$, $\beta = 2.9971\times10^6 - 3.3188/\lambda_{1,2}$ and $\gamma = -4.2214\times10^6 - 7.2467/\lambda_{1,2}$ depend on the wavelength. The results derived with Eq. (11) are shown in Fig. 3 by dash curves. The average percentage differences between the simulated and fitted data are 4.7292% and 3.4971% respectively for 1480 and 1550 nm.

3.2. Simulation results for the RI region 1.00–1.50

In a narrower region 1.00–1.50 of RI values, a linear dependence of the splitting ratio can be chosen for our RI sensor (see Fig. 4). The splitting ratio at the operating wavelength 1480 nm increases from 1.00 up to 1.14 when the RI increases from 1.00 to 1.50. The sensitivity is equal to 0.2653 RIU^{-1} and we have the goodness-of-fit $R^2 = 0.9889$. At the operating wavelength 1550 nm, the splitting ratio decreases from 1.00 to 0.76. Here we have the sensitivity 0.4908 RIU^{-1}, of which tendency is the opposite to the case of 1480 nm, and $R^2 = 0.9777$.

A linear relationship between the splitting ratio at both operating wavelengths and the RI can be represented as

$$Splitting\ ratio(n,\lambda) = \left(\delta n + \varepsilon\right)\lambda, \tag{12}$$

where $\delta = -1.0782\times10^7 + 16.2239/\lambda_{1,2}$ and $\varepsilon = 1.0554\times10^7 - 14.8888/\lambda_{1,2}$ are the wavelength-dependent parameters.

The results of fitting performed using Eq. (12) are shown by the dash curves in Fig. 4. The average percentage differences between the simulated splitting ratios and the fitting data are 0.3150% and 1.2046%, respectively.

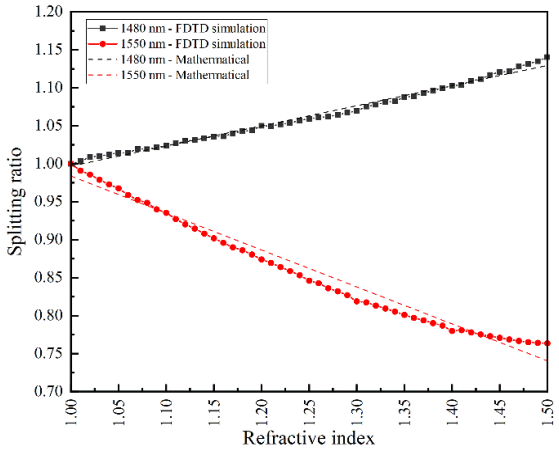

Fig. 4. Simulated splitting ratios as functions of RI in the region 1.00–1.50: black squares and red circles correspond respectively to the operating wavelengths 1480 and 1550 nm, and dash curves are the data calculated with Eq. (12).

3.3. Optical transmissions at the output ports of ultrawide-range RI sensor

Fig. 5 shows dependences of the simulated optical transmissions at the two output ports on the RI at the two operating wavelengths. As seen from Fig. 5a, the optical transmissions at the output ports calculated at the wavelength 1480 nm become equal to each other when the RI of the sensing area is 1.00. The optical transmission at the output port 1 increases with increasing RI, while the transmission at the output port 2 decreases under this condition. The maximal optical transmission at the port 1 amounts to 53.28% and the minimal optical transmission at the port 2 is 46.72%.

Fig. 5b shows the results of simulations performed at the operating wavelength 1550 nm. The optical transmissions at both output ports are the same at the unit RI of the rod-like sensing area. The optical transmission at the port 1 decreases and the transmission at the port 2 increases with increasing RI. The minimal transmission at the port 1 is equal to 43.30% and the maximal transmission at the port 2 is 56.70%.

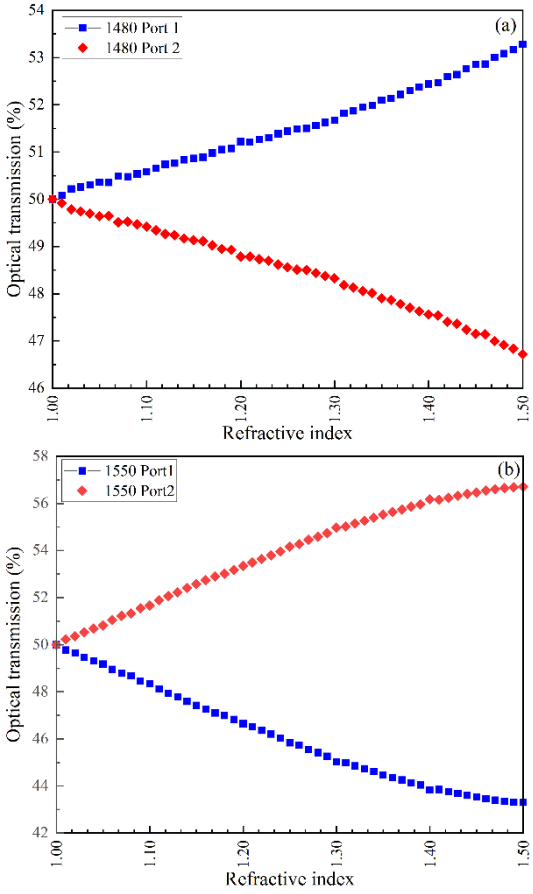

Fig. 5. Optical transmissions at the output ports 1 and 2 simulated with the FDTD method as functions of RI at the operating wavelengths 1480 nm (a) and 1550 nm (b). Blue and red lines correspond to the output ports 1 and 2, respectively (see the legend).

Using Eq. (10), we have analyzed the coupling coefficient for the region of linear dependence of the transmission on the RI n and obtained the relations $\kappa_{\lambda 1} = 0.56258 - 0.062154n$ and $\kappa_{\lambda 2} = 0.36301 + 0.14072n$.

One can notice different responses of our sensor at different operating wavelengths (compare the simulation results shown in Fig. 5a and Fig. 5b). The optical transmission at the output port 1 either increases (at 1480 nm) or decreases (at 1550) nm with increasing RI. The situation observed for the output port 2 is the opposite. Here the optical transmission decreases at the operating wavelength 1480 nm and increases at the wavelength 1550 nm.

3.4. Field distribution and comparison of performances of different IR sensors

Fig. 6 shows spatial distributions of the electric field inside the *XZ* plane, which have been obtained at different RI values of the rod-like sensing area. Note that the panels (a) to (c) of Fig. 6 correspond to the splitting ratios 1.0235, 1.0693 and 1.1405, respectively. Finally, the panels (d) to (f) in Fig. 6 refer respectively to the splitting ratios 0.9354, 0.8189 and 0.7637.

In Table 1 we compare the fundamental principles and the specific characteristics of different RI sensors, including our sensor. The RI sensors reported in Refs. [8, 10, 14] are based on the spectral-shift mechanism. The widest measurement range of these sensors is 0.052 RIU and the average measurement range is approximately equal to 0.028 RIU. On the other hand, the RI sensors described in Refs. [18–21] are based on the intensity-shift mechanism. Here the widest measurement range is given by 0.082 RIU, while the average range is equal to about 0.039 RIU.

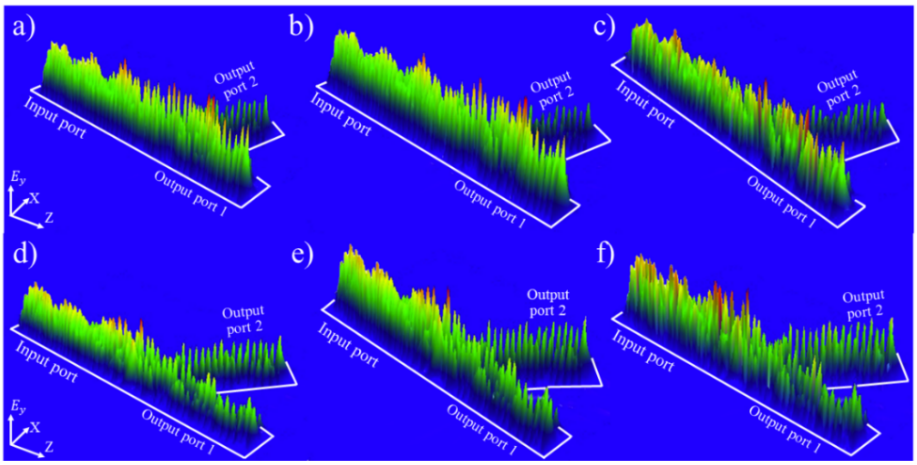

Fig. 6. Electric-field distributions observed at different RI values of the rod-like sensing area: panels (a) to (c) correspond respectively to n = 1.10, 1.30 and 1.50 (the operating wavelength 1480 nm) and panels (d) to (f) to n = 1.10, 1.30 and 1.50 (the operating wavelength 1550 nm).

Some other wide- or ultrawide-range RI sensors have been introduced in the works [34, 35]. In Ref. [34], an ultrawide-range RI sensor with the measurement range 1.00–1.80 has been reported, which can be operated using a light source with the spectral width 1500 nm. The calculated sensitivity of this sensor amounts to 1002 nm/RIU. The authors [35] have introduced a wide-range RI sensor with the measurement range 1.29–1.49 RIU and a light source with the spectral width 1000 nm. The sensitivities calculated for this sensor are –4156.82 and –3703.64 nm/RIU for the *x*- and *y*-polarized modes, respectively. These RI sensors are based on the spectral-shift mechanism. Note that a broadband source and an optical spectrum analyzer with a wide operation range are required in this case.

Table 1. Comparison of working principles and parameters of different RI sensors.

Reference	Structure type	Sensing mechanism	Operating wavelength, nm	RI range	Sensitivity
This work	Asymmetric Y-junction	Intensity shift	1480	1.00–1.50	0.2653 RIU^{-1}
			1550		–0.4908 RIU^{-1}
[8]	Mach–Zehnder interferometers	Spectral shift	1450–1650	1.3320–1.3840	415 nm/RIU
				1.3840–1.4204	1103 nm/RIU
				1.4204–1.4408	4234 nm/RIU
[10]	Photonic crystals	Spectral shift	2020–2100	1.00026–1.00046	1.9×10^5 nm/RIU
[14]	Surface plasmon resonance	Spectral shift	350–1100	1.3353–1.3653	1600 nm/RIU
[18]	Long-period fibre grating	Intensity shift	1460	1.33–1.38	31 dB/RIU
				1.38–1.42	47 dB/RIU
[19]	Plastic optical fibre	Intensity shift	660	1.33–1.41	10^{-3}–10^{-4} RIU
[20]	SNHNS	Intensity shift	1550.10	1.334–1.384	–367.9 dB/RIU
[21]	TMDM	Intensity shift	1540	1.330–1.339	516.02 dB/RIU
				1.330–1.356	965.46 dB/RIU
[34]	Surface plasmon resonance	Spectral shift	500–2000	1.00–1.80	1002 nm/RIU
[35]	Photonic crystal fibre	Spectral shift	1000–2000	1.29–1.49	–4156.82 nm/RIU –3703.64 nm/RIU

A comparison of the sensors mentioned in Table 1 testifies that we have provided a novel design of the RI sensor, which is characterized by an ultrawide measurement range, the intensity-shift mechanism and simple equipment. The sensor offered in the present work needs only a laser diode operating at two different wavelengths and a photodetector. It enables detecting various biochemical or chemical specimens with the RI values lying in the region 1.00–1.50. Moreover, a gas sensor or a biosensor can be designed as a compact-size device. The process of identification can be performed rapidly by comparing the splitting ratios at both operating wavelengths. To improve the accuracy of the sensor, a multi-sensing structure can be built (see Fig. 7). In particular, its sensitivity can be increased by improving performance of the electronic part of photodetecting section.

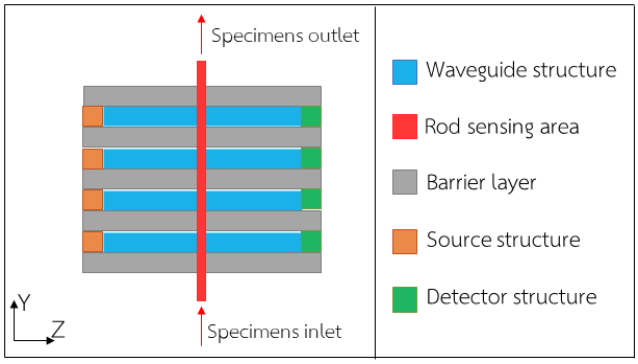

Fig. 7. Schematic design of a possible multi-sensing structure.

4. Conclusion

We present a novel design for an ultrawide-range optical RI sensor, which is based on an asymmetric Y-junction optical splitter built on InP. The operation of the sensor has been simulated at the optical wavelengths 1480 and 1550 nm. The results of simulations carried out with the FDTD method reveal a quadratic dependence of the splitting ratio on the RI in the IR range 1.00–

2.50. An approximately linear dependence holds true in a narrower RI region, 1.00–1.50. The sensitivities of our sensor in this region are equal to 0.2653 and –0.4908 RIU^{-1} respectively at the operating wavelengths 1480 and 1550 nm, with the R^2 parameters amounting to 0.9889 and 0.9777. We have also analyzed the coupling coefficient as a function of the RI at both operating wavelengths. The appropriate dependences are given by $\kappa_{\lambda 1} = 0.56258 - 0.062154n$ and $\kappa_{\lambda 2} = 0.36301 + 0.14072n$. The device suggested by us can be used as an ultrawide-range RI sensor which employs the intensity-shift concept and reveals the measurement region 1.00–1.50 for the IR. It enables real-time sensing of various biochemical or chemical specimens and can be applied in different medical and industrial fields. Moreover, our sensor is characterized by a very simple design and moderate demands to the optical and electronic equipment involved.

Funding. This research received no external funding.

Disclosures. The authors declare no conflicts of interest.

References

1. Dinh T-V, Choi I Y, Son Y-S and Kim J-C, 2016. A review on non-dispersive infrared gas sensors: Improvement of sensor detection limit and interference correction. Sens. Act. B: Chem. **231**: 529–538.
2. Nazemi H, Joseph A, Park J and Emadi A, 2019. Advanced micro- and nano-gas sensor technology: a review. Sensors **19**: 1285.
3. Goldenstein C S, Spearrin R M, Jeffries J B and Hanson R K, 2017. Infrared laser-absorption sensing for combustion gases. Prog. En. Comb. Sci. **60**: 132–176.
4. Ranacher C, Consani C, Tortschanoff A, Jannesari R, Bergmeister M, Grille T and Jakoby B, 2018. Mid-infrared absorption gas sensing using a silicon strip waveguide. Sens. Act. A: Phys. **277**: 117–123.
5. Popa D and Udrea F, 2019. Towards integrated mid-infrared gas sensors. Sensors. **19**: 2076.
6. Chu R, Guan C, Bo Y, Shi J, Zhu Z, Li P, Yang J and Yuan L, 2019. All-optical graphene-oxide humidity sensor based on a side-polished symmetrical twin-core fiber Michelson interferometer. Sens. Act. B: Chem. **284**: 623–627.
7. Ahsani V, Ahmed F, Jun M B G and Bradley C, 2019. Tapered fiber-optic Mach–Zehnder interferometer for ultra-high sensitivity measurement of refractive index. Sensors. **19**: 1652.
8. Sun B, Chen M-Y, Zhang Y-K and Yang J-C, 2012. Design of refractive index sensors based on the wavelength-selective resonant coupling phenomenon in dual-core photonic crystal fibers. J. Biomed. Opt. **17**: 037002,
9. Zaky Z A, Ahmed A M, Shalaby A S and Aly A H, Refractive index gas sensor based on the Tamm state in a onedimensional photonic crystal: theoretical optimization. Sci. Rep. **10**: 9736.
10. Srinuanjan K, Kamoldilok S, Tipaphong W and Yupapin P P, 2011. A nano-scale transducer using a PANDA type ring resonator for gas sensor applications. Optik. **123**: 475–478.
11. Gao B, Wang Y, Zhang T, Xu Y, He A, Dai L and Zhang J, 2019. Nanoscale refractive index sensors with high figures of merit via optical slot antennas. ACS Nano. **13**: 9131–9138.
12. Bello V, Simoni A and Merlo S, 2020. Spectral phase shift interferometry for refractive index monitoring in microcapillaries. Sensors. **20**: 1043.
13. Wang P, Zhang L, Xia Y, Tong L, Xu X and Ying Y, 2012. Polymer nanofibers embedded with aligned gold nanorods: a new platform for plasmonic studies and optical sensing. Nano Lett. **12**: 3145−3150.

14. Al-Qazwini Y, Noor A S M, Yaacob M H, Harun S W and Mahdi M A, 2015. Fabrication and characterization of a refractive index sensor based on SPR in an etched plastic optical fiber. Proc. Engin. **120**: 969–974.
15. Dormeny A A, Sohi P A and Kahrizi M, 2020. Design and simulation of a refractive index sensor based on SPR and LSPR using gold nanostructures. Res. Phys. **16**: 102869.
16. Dong M, Zheng C, Miao S, Zhang Y, Du Q, Wang Y and Tittel F K, 2017. Development and measurements of a mid-infrared multi-gas sensor system for CO, CO_2 and CH_4 detection. Sensors. **17**: 2221.
17. Gervais A, Jean P, Shi W and LaRochelle S, 2019. Design of slow-light subwavelength grating waveguides for enhanced on-chip methane sensing by absorption spectroscopy. IEEE J. Select. Top. Quant. Elect. **25**: 5200308.
18. Tan C, Ji W B, Mamidala V, Chow K K and Tjin S C, 2014. Carbon-nanotube-deposited long period fiber grating for continuous refractive index sensor applications. Sens. Act. B: Chem. **196**: 260–264.
19. Sequeira F, Cennamo N, Rudnitskaya A, Nogueira R, Zeni L and Bilro L, 2019. D-shaped POF sensors for refractive index sensing – the importance of surface roughness. Sensors. **19**: 2476.
20. Yin B, Wu S, Wang M, Liu W, Li H, Wu B and Wang Q, 2019. High-sensitivity refractive index and temperature sensor based on cascaded dual-wavelength fiber laser and SNHNS interferometer. Opt. Express. **27**: 252–264.
21. Li Z, Hou L, Ran L, Kang J and Yang J, 2019. Ultra-sensitive fiber refractive index sensor with intensity modulation and self-temperature compensation. Sensors. **19**: 3820.
22. Gu F, Zhang L, Yin X and Tong L, 2008. Polymer single-nanowire optical sensors. Nano Lett. **8**: 2757–2761.
23. Qin J, Chen Y-H, Ding B, Blaikie R J, Qiu M, 2017. Efficient plasmonic gas sensing based on cavity-coupled metallic nanoparticles. J. Phys. Chem. C. **121**: 24740–24744.
24. Lee C W, Suh J M and Jang H W, 2019. Chemical sensors based on two-dimensional (2D) materials for selective detection of ions and molecules in liquid. Front. Chem. **7**: 708.
25. Yang L C, Huang C-C, Huang H-C and Tsao S-L, 2011. A novel 1×2 optical power splitter with PBG structures on SOI substrate. Optik. **123**: 306–309.
26. Chantakit T, Srinuanjan K and Yupapin P P, 2014. Two dimension photonic crystal Y-branch beam splitter with variation of splitting ratio based on hybrid defect controlled. Appl. Phys. A. **117**: 547–552.
27. Ab-Rahman M S, Aziz A N A, Nordin R, Jumari K, 2020. Optimum design of an optical waveguide: determination of the branching angle of s-bend waveguides. Optik. **200**: 163249.
28. Gašo P, Pudiš D, Seyringer D, Kuzma A, Gajdošová L, Mizera T and Goraus M, 2020. 3D polymer based 1×4 beam splitter. J. Lightwave Technol. **39**: 154–161.
29. Kawano K and Kitoh T. Introduction to Optical Waveguide Analysis. New York: John Wiley &Sons, 2001.
30. Okamoto K. Fundamentals of Optical Waveguides. Elsevier Inc, 2006.
31. Wheeler A J and Ganji A R, Introduction to Engineering Experimentation. New Jersey: Pearson Education, 2010.
32. Phongwisit P, Kamoldilok S, Buranasiri P, Srinuanjan K and Limsuwan P, 2022. Design and simulation of asymmetric Y-junction beam splitter with controllable splitting based on adjusted air-hole defect. Ukr. J. Phys. Opt. **23**: 142–149.

33. Smirnova A, Shimizu H, Pihosh Y, Mawatari K and Kitamori T, 2016. On-chip step-mixing in a T-nanomixer for liquid chromatography in extended-nanochannels. Anal. Chem. **88**: 10059−10064.
34. Wang X, Zhu J, Wen X, Wu X, Wu Y, Su Y, Tong H, Qi Y and Yang H, 2019. Wide range refractive index sensor based on a coupled structure of Au nanocubes and Au film. Opt. Mater. Express. **9**: 3079–3088.
35. Wang G, Lu Y, Duan L and Yao J, 2021. A refractive index sensor based on PCF with ultra-wide detection range. IEEE J. Select. Top. Quant. Electr. **27**: 5600108.

Phongwisit P., Kamoldilok S., Limsuwan P. and Srinuanjan K. 2023. Ultrawide-range refractive-index sensor based on asymmetric integrated Y-junction optical waveguide. Ukr.J.Phys.Opt. 24: 161 – 171. doi: 10.3116/16091833/24/2/161/2023

Анотація. *Описано новий сенсор показника заломлення (ПЗ) із надширoким робочим діапазоном на основі асиметричного оптичного подільника з Y-подібним з'єднанням. Стрижень циліндричної форми з діаметром 350 нм і висотою 1000 нм, який має інший ПЗ, вставляють у спай асиметричного хвилеводу з Y-подібним з'єднанням. Цей стрижень служить чутливою зоною. Виконано моделювання сенсора за допомогою методу скінченних різниць у часовій області. Досліджено коефіцієнт розщеплення для двох робочих довжин хвиль 1480 і 1550 нм. Результати показують, що коефіцієнт розщеплення на обох робочих довжинах хвилі можна описати як параболічну функцію ПЗ чутливої зони. Наближено лінійна залежність між коефіцієнтом розщеплення та ПЗ має місце для вужчої області ПЗ 1,00–1,50, що дає змогу розробити сенсор ПЗ із надширoким діапазоном. Чутливості сенсора на довжинах хвиль 1480 і 1550 нм дорівнюють відповідно 0,2653 і –0,4908 RIU^{-1}, а відповідні параметри R^2 складають 0,9889 і 0,9777. Наш пристрій може слугувати оптичним сенсором ПЗ із надширoким робочим діапазоном для ідентифікації мікроскопічних біохімічних або хімічних зразків.*

Ключові слова: *датчики показника заломлення, сенсори із зсувом інтенсивності, хвилеводи з Y-подібним з'єднанням, інтегрована фотоніка.*